



# An online heat generation estimation method for lithium-ion batteries using dual-temperature measurements

Jianan Zhang<sup>a,b,c</sup>, Xiao-Guang Yang<sup>b</sup>, Fengchun Sun<sup>a,c</sup>, Zhenpo Wang<sup>a,c,\*</sup>, Chao-Yang Wang<sup>b,\*</sup>

<sup>a</sup> National Engineering Laboratory for Electric Vehicles, Beijing Institute of Technology, Beijing 100081, China

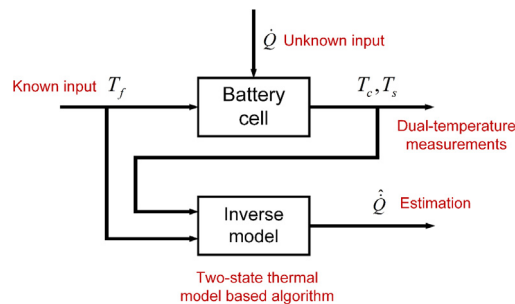
<sup>b</sup> Electrochemical Engine Center (ECEC) and Department of Mechanical Engineering, The Pennsylvania State University, University Park, PA 16802, USA

<sup>c</sup> Collaborative Innovation Center for Electric Vehicles in Beijing, Beijing 100081, China

## HIGHLIGHTS

- A straightforward and accurate Li-ion battery heat generation estimation method is presented for online usage.
- The method is of strong robustness against changes in ambient temperatures and convection conditions.
- Heat generation inside a battery cell regardless of sources are covered.

## GRAPHICAL ABSTRACT



## ARTICLE INFO

### Keywords:

Lithium-ion battery  
Heat generation estimation  
Temperature measurement  
Thermal model

## ABSTRACT

Estimation of heat generation in lithium-ion batteries (LiBs) is critical for enhancing battery performance and safety. Here, we present a method for estimating total heat generation in LiBs based on dual-temperature measurement (DTM) and a two-state thermal model, which is both accurate and fast for online applications. We demonstrate that the algorithm can keep track of the heat generation rate in real-time under scenarios of designed multi-stepwise heat generation profile and regular fast charging processes. Moreover, the algorithm requires no knowledge of the thermal boundary conditions, providing robustness against changes in convection conditions and ambient temperatures. Finally, this method can capture heat generation induced by abnormal exothermic reactions, which could be a useful tool for detection of battery thermal failures.

## 1. Introduction

The performance, durability, and safety of lithium-ion batteries (LiBs) are all closely related to their thermal behaviors [1]. Estimation of heat generation onboard is critical for understanding the thermal behaviors of LiBs and for devising strategies to enhance battery life and safety.

Previous efforts of battery heat generation determination are mostly

experimental. Therein, calorimetry is a favorable approach. Accelerating rate calorimetry (ARC) [2,3], isothermal heat conduction calorimetry (IHC) [4], and improved high precision calorimeter [5] are reported to explore battery thermal behavior. Moreover, unconventional methods such as a multi-sensor fusion method with heat flux measurement [6] have been designed for the *in-situ* estimation. However, these methods are only applicable in laboratory conditions and difficult to be implemented to onboard applications, such as electric

\* Corresponding authors at: Electrochemical Engine Center (ECEC) and Department of Mechanical Engineering, The Pennsylvania State University, University Park, PA 16802, USA (C-Y Wang); National Engineering Laboratory for Electric Vehicles, Beijing Institute of Technology, Beijing 100081, China (Z. Wang).

E-mail addresses: [wangzhenpo@bit.edu.cn](mailto:wangzhenpo@bit.edu.cn) (Z. Wang), [cwx31@psu.edu](mailto:cwx31@psu.edu) (C.-Y. Wang).

<https://doi.org/10.1016/j.apenergy.2020.115262>

Received 24 December 2019; Received in revised form 23 April 2020; Accepted 24 May 2020

0306-2619/© 2020 Published by Elsevier Ltd.

Nomenclature	
<i>Electrochemical-thermal model</i>	
$A_e$	electrode area ( $\text{m}^2$ )
$c$	lithium concentration ( $\text{mol m}^{-3}$ )
$c_p$	specific heat ( $\text{J kg}^{-1} \text{K}^{-1}$ )
$D$	diffusivity ( $\text{m}^2 \text{s}^{-1}$ )
$F$	Faraday constant ( $96487 \text{ C mol}^{-1}$ )
$h$	convective heat transfer coefficient ( $\text{W m}^{-2} \text{K}^{-1}$ )
$j$	volumetric current density ( $\text{A m}^{-3}$ )
$L$	sum of the anode, separator and cathode thicknesses (m)
$\dot{Q}$	total heat generation rate (W)
$\dot{Q}_{app}$	applied additional heat generation rate (W)
$\dot{Q}_{ele}$	electrochemical heat generation rate (W)
$r$	coordinate in the radial direction (m)
$t$	time (s)
$t_+$	transference number
$T$	temperature (K)
$U$	open circuit potential (V)
$x$	coordinate in the electrode thickness direction (m)
$z$	coordinate in the cell thickness direction (m)
<i>Greek</i>	
$\varepsilon$	volume fraction
$\delta$	cell thickness (m)
$\kappa$	thermal conductivity ( $\text{W m}^{-1} \text{K}^{-1}$ )
$\kappa^{eff}$	effective ionic conductivity ( $\text{S m}^{-1}$ )
$\kappa_D^{eff}$	effective diffusional ionic conductivity ( $\text{S m}^{-1}$ )
$\rho$	density ( $\text{kg m}^{-3}$ )
$\sigma^{eff}$	effective electronic conductivity ( $\text{S m}^{-1}$ )
$\phi$	phase potential (V)
<i>Superscript and subscripts</i>	
avg	average
$e$	electrolyte phase
$s$	solid phase
<i>Two-state thermal model</i>	
$C_c$	heat capacity of the battery cell core component ( $\text{J K}^{-1}$ )
$C_s$	heat capacity of the battery cell surface component ( $\text{J K}^{-1}$ )
$\dot{\hat{Q}}$	total heat generation rate (W)
$\hat{\dot{Q}}$	estimated total heat generation rate (W)
$R_c$	thermal resistance between the core and the surface component ( $\text{K W}^{-1}$ )
$R_u$	convective thermal resistance between the surface component and ambient ( $\text{K W}^{-1}$ )
$\Delta t$	sampling interval
$T_c$	core temperature (K)
$T_s$	surface temperature (K)
<i>Superscript and subscripts</i>	
$k$	$k$ th time step
<i>List of abbreviations</i>	
ACT	activation
DTM	dual-temperature measurement
ECT	electrochemical-thermal
EV	electric vehicle
FUDS	Federal Urban Driving Schedule
ITS	internal temperature sensor
OCV	open circuit voltage
PSO	particle swarm optimization
RMSE	root mean squared error
SHLB	self-heating lithium-ion battery
SOC	state of charge

vehicles (EVs).

On the other hand, in order to capture heat generation, modeling methods have been used in the existing literature. The electrochemical-thermal (ECT) models based on physical principles can calculate heat generation, including kinetic heat, reversible heat, joule heat, etc. [7,8] with excellent accuracy. However, they require high computational costs and are difficult to be implemented in real-world applications.

Therefore, simplified methods are utilized in online situations. Constant heat generation rate [9], curve fitting technique [10], and Joule's Law [11] are extensively used in engineering practices. Nevertheless, these approaches can be over-simplified and lead to significant errors or a lack of generalization capabilities. Beyond those, the most used method to date is the simplified equation deduced by Bernardi [2], which calculates heat generation via  $I^*(OCV - V_{cell})$ , where  $I$  is current,  $OCV$  is open-circuit voltage, and  $V_{cell}$  is cell voltage. However, due to the necessity of voltage, current, open circuit voltage (OCV), and state of charge (SOC), the high estimation accuracy is required for these primary parameters, and significant errors could occur in practice. In addition, the modeling methods consider heat generation from known electrochemical sources via given electrochemical processes or equations. Hence, unmodeled heat generation behavior or abnormal heat generation, such as internal short circuits and exothermic side reactions, are unable to be accounted for.

To resolve the drawbacks of existing experimental and modeling approaches and to address the convenience and accuracy required of onboard applications, better understanding of battery thermal behavior

is necessary. Also, as automotive battery cells become large in size, there is usually a significant temperature gradient inside a cell [12]. Therefore, obtaining internal temperatures become necessary. Methods such as impedance-based estimation by its temperature dependency [13], model-based estimation algorithm with Kalman filter techniques [14], or direct measurement using embedded thermal couples [15] have been widely reported. However, gaining knowledge of internal temperature is rather limited, and most of the methods mentioned above are impossible for use in onboard applications.

In this paper, we present a direct and accurate method to estimate battery heat generation in real-time from a heat transfer perspective. In order to handle the problem of temperature gradient inside a cell, a dual-temperature measurement (DTM) structure is proposed. It is motivated by the self-heating lithium-ion battery (SHLB) [16] and can measure battery surface and core temperatures simultaneously. The SHLB has a micron-thin nickel (Ni) foil embedded in the center of a cell, whose resistance is linear with respect to temperature and can thus serve as an internal temperature sensor (ITS). More details about the SHLB structure is given in Section 3.1. Afterward, the temperatures measured by DTM are incorporated into a two-state thermal model to estimate heat generation, which achieves a good balance between accuracy and computational cost. The heat generation estimation algorithm is developed by utilizing discretization and inverse model techniques. It can be observed that the proposed algorithm requires no prior knowledge of thermal boundary conditions and also exhibits strong robustness against changes in thermal boundary conditions. Moreover,

the total heat generation of a battery cell is obtained. Thus, abnormal heat generation can be detected from the estimation results, which is valuable for early detection of thermal faults and improved battery safety.

In order to demonstrate the accuracy of the presented method, a series of simulations are conducted through an experimentally calibrated ECT coupled model under conditions of a hypothetically designed multi-stepwise heat generation profile and heat generation in fast charging cases. The heat generation rates resulting from the ECT model are taken as theoretical values and are compared with the algorithm estimation values. In addition, the effects of heat convection conditions and cell thicknesses are explored.

The remainder of this paper is organized as follows: the ECT modeling is presented in Section 2. Section 3 introduces the present heat generation estimation scheme. Section 4 shows the simulation results and algorithm evaluation. Section 5 concludes the paper.

## 2. Electrochemical-thermal model

In this section, an electrochemical-thermal (ECT) model is developed, which will be used to generate necessary data for parameter identification of the two-state thermal model and will be employed for evaluation of estimation results. The ECT model is established in GT-AutoLion™, a commercial software package for multi-disciplinary lithium-ion battery and system simulation and analysis [17]. Moreover, the ECT model is validated against experimental results, which are shown in the Appendix A. Charge/discharge with different C-rates and temperature tests are validated respectively in Figs. A1–A3.

In this research, the modeled lithium-ion battery is a 10Ah pouch cell, with electrode chemistry of  $\text{LiNi}_{0.6}\text{Mn}_{0.2}\text{Co}_{0.2}\text{O}_2$  (NMC622)/Graphite and the electrolyte of 1 M  $\text{LiPF}_6$  in 3:7 (wt%/wt%) EC/EMC with 2% wt VC. The dimension of the cell is 130 mm \* 75 mm \* 10 mm (length \* width \* thickness).

### 2.1. Electrochemical model

By adopting the fully coupled electrochemical model of Gu and Wang [18], the conservation equations are given by the following Eqs. (1)–(4):

Charge conservation in solid electrodes:

$$\nabla \cdot (\sigma_s^{\text{eff}} \nabla \phi_s) = j \quad (1)$$

where  $\sigma_s^{\text{eff}}$  is the effective electronic conductivity of solid phase,  $\phi_s$  is the electric potential in solid phase, and  $j$  is the volumetric current density.

Charge conservation in electrolyte:

$$\nabla \cdot (\kappa_D^{\text{eff}} \nabla \phi_e) + \nabla \cdot (\kappa_D^{\text{eff}} \nabla \ln c_e) = -j \quad (2)$$

where  $\kappa^{\text{eff}}$  is the effective ionic conductivity of electrolyte,  $\phi_e$  is the electric potential in electrolyte,  $\kappa_D^{\text{eff}}$  is the effective diffusional ionic conductivity of electrolyte,  $c_e$  is the species concentration in electrolyte.

Species conservation in electrolyte:

$$\varepsilon \frac{\partial c_e}{\partial t} = \nabla \cdot (D_e^{\text{eff}} \nabla c_e) + \frac{1-t_+}{F} j \quad (3)$$

in which  $\varepsilon$  is the volume fraction,  $D_e^{\text{eff}}$  is the effective electrolyte diffusivity,  $t_+$  is the transference number,  $F$  is the Faraday constant.

Species conservation in active material particles:

$$\frac{\partial c_s}{\partial t} = \frac{1}{r^2} \frac{\partial}{\partial r} \left( D_s r^2 \frac{\partial c_s}{\partial r} \right) \quad (4)$$

in which  $c_s$  is the species concentration in solid phase and  $D_s$  is the solid phase diffusivity,  $r$  is the coordinate in the particle radial direction,  $t$  is the time.

Detailed explanations of the above equations can also be found in the literature [19,20] and therefore are not repeated here. Parameters of these equations are adopted from the materials database of GT-

AutoLion™.

### 2.2. Thermal model

For depicting the heat transfer process of a battery cell, a 1D thermal model is adopted [21]. Governing equations for the thermal field are given below.

Thermal energy conservation:

$$\rho c_p \frac{\partial T}{\partial t} = \nabla \cdot (\kappa \nabla T) + \dot{Q} \quad (5)$$

where  $\rho$ ,  $c_p$  and  $\kappa$  are density, specific heat capacity, and thermal conductivity of the cell, respectively,  $\dot{Q}$  is the heat generation term. Thermal properties of the pouch battery cell, such as specific heat capacity and thermal conductivity are employed from the literature [22].

Thermal boundary conditions:

$$\frac{\partial T}{\partial z}(0, t) = 0 \quad (6)$$

$$\frac{\partial T}{\partial z}(\delta, t) = \frac{h}{\kappa} [T_\infty - T(\delta, t)] \quad (7)$$

where  $t$  stands for time, and  $z \in [0, \delta]$  is the spatial coordinate in the battery cell thickness direction. The origin of the coordinate system lies in the middle of the cell thickness and  $\delta$  represents half of the cell thickness.  $h$  is the convective heat transfer coefficient.

Heat generation from electrochemical effects is given as [18]:

$$\begin{aligned} \dot{Q}_{ele} &= A_e \int_0^L \left[ j \left( T_{\text{avg}} \frac{\partial U}{\partial T_{\text{avg}}} \right) + j(\phi_s - \phi_e - U) + \sigma_s^{\text{eff}} \nabla \phi_s \cdot \nabla \phi_s + \kappa^{\text{eff}} \nabla \phi_e \cdot \nabla \phi_e \right. \\ &\quad \left. + \kappa_D^{\text{eff}} \nabla \ln c_e \cdot \nabla \phi_e \right] dx \end{aligned} \quad (8)$$

where  $A_e$  is the electrode area,  $L$  is the sum of the anode, separator, and cathode thickness,  $T_{\text{avg}}$  is the average temperature of the battery cell.

The  $j \left( T_{\text{avg}} \frac{\partial U}{\partial T_{\text{avg}}} \right)$  term shows the reversible heat, the  $j(\phi_s - \phi_e - U)$  term represents kinetic heat, the  $\sigma_s^{\text{eff}} \nabla \phi_s \cdot \nabla \phi_s$ ,  $\kappa^{\text{eff}} \nabla \phi_e \cdot \nabla \phi_e$  and  $\kappa_D^{\text{eff}} \nabla \ln c_e \cdot \nabla \phi_e$  term indicates joule heat from electronic resistance, ionic resistance and concentration overpotential, respectively. More detailed explanations for the above heat generation equation can also be referred to Ref. [19].

### 2.3. Treatment of performing extra given heat generation rate

Battery normal heat generation is a result of the loading current during operation. However, the amplitude of the electrochemical heat generation rate also depends on cell dimensions, SOCs, and even cell temperatures. In order to provide an unbiased comparison and discussion between different case studies, a consistently designed heat generation profile is needed, and an extra given heat generation rate  $\dot{Q}_{app}$  is applied to compose the total heat generation of the battery cell. Therefore, the total heat generation rate is given by:

$$\dot{Q} = \dot{Q}_{ele} + \dot{Q}_{app} \quad (9)$$

Note that when battery cell has no current flowing through,  $\dot{Q}_{ele} = 0$ , and hence  $\dot{Q} = \dot{Q}_{app}$ .

## 3. Heat generation estimation scheme

### 3.1. Dual-temperature measurement method

In this subsection, a dual-temperature measurement (DTM) method is presented, which provides necessary core and surface temperature information for estimation of the battery heat generation. DTM is implemented via the SHLB structure elaborated earlier [16].

In brief, SHLB is a novel battery structure developed and researched in the past few years, as shown in Refs. [16,23]. It can perform self-heating and take a battery from sub-freezing temperatures to its optimal operating range within tens of seconds. The structural design of SHLB is shown in Fig. 1a. A thin piece of nickel (Ni) foil is embedded in the center of a pouch cell. One end of the Ni foil is welded with the anode tabs and connected to the negative terminal; the other end extends outside the cell to form a third terminal called the activation (ACT) terminal. A switch is added in between the positive and ACT terminals. When the switch is closed (see Fig. 1b), a large current will flow through the Ni foil, creating immense and uniform heat that can rapidly warm up the battery.

In addition to the capability of rapid heating, the embedded Ni foil provides as the function of an internal temperature sensing (ITS) as the foil resistance linearly varies with temperature [24], as plotted in Fig. 1c. Additionally, a cell's surface temperature can be readily obtained with routine methods such as thermocouples or thermal-resistors. Consequently, the DTM structure can be realized with the combination of both core and surface temperature measurements.

### 3.2. Two-state thermal model

In tandem with the dual-temperature measurements, a two-state thermal model is employed for the heat generation estimation scheme. On one hand, compared with a differential equation thermal model, the two-state thermal model is only composed of two lumped components and therefore is more efficient for online applications. On the other hand, the two-state thermal model can capture better cell heat transfer behavior than the single-state lumped model for EV type battery cells, of which the Biot number is large and therefore significant temperature difference arises between the battery core and surface. In such a case, the single-state lumped model would be inaccurate. A two-state thermal model was firstly developed for cylindrical cells [25], and was more recently utilized for e.g. battery fault diagnosis [26] and capacity estimation [27]. In this study, the model is extended to accommodate a pouch cell configuration. The schematic of the two-state model for pouch cell is shown in Fig. 2.

In the two-state thermal model, there are two lumped parts: the core component, which stands for electrode/separator stacks, and the surface component, which stands for cell package. Core temperature,  $T_c$ , and surface temperature,  $T_s$ , are the two states of the system. Heat transfer features are modeled as a conductive thermal resistance between the core and the surface components, denoted as  $R_c$ , and a convective thermal resistance between the surface component and the ambient, denoted as  $R_u$ .  $C_c$  and  $C_s$  are heat capacity of the core and surface component, respectively.  $T_f$  is the temperature of the ambient air/liquid flow. The heat generation rate, denoted as  $\dot{Q}$ , occurs only in the cell core component, which complies with the real cases. The

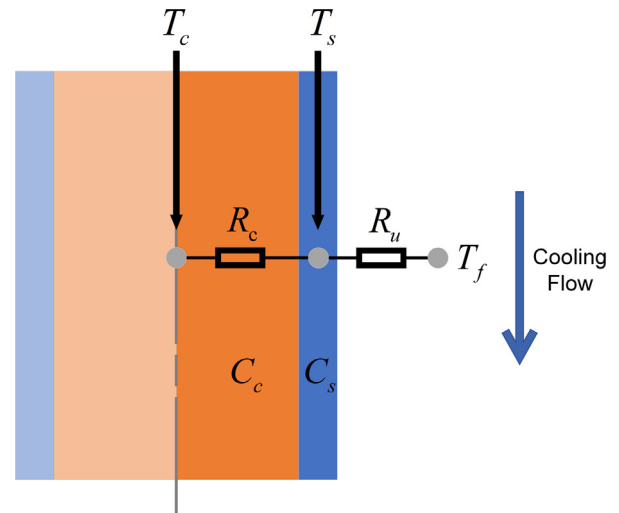


Fig. 2. Schematic of the two-state thermal model.

governing equations of the two-state thermal model are shown in Eqs. (10) and (11):

$$C_c \dot{T}_c = \frac{T_s - T_c}{R_c} + \dot{Q} \tag{10}$$

$$C_s \dot{T}_s = -\frac{T_s - T_c}{R_c} + \frac{T_f - T_s}{R_u} \tag{11}$$

### 3.3. Heat generation estimation algorithm

In this subsection, the heat generation estimation algorithm is presented with the proposed two-state thermal model using discretization and inverse model techniques.

The normal two-state thermal model takes the ambient temperature  $T_f$  and heat generation rate  $\dot{Q}$  as inputs and gives core temperature  $T_c$  and surface temperature  $T_s$  as outputs. On the contrary, in our task, the heat generation rate is to be solved. This situation yields an unknown input reconstruction problem, which can be described as: the known input (heat generation rate) needs to be reconstructed using the information of measured outputs (core and surface temperatures) and the known input (ambient temperature).

Therefore, to address the issue, the two-state thermal model needs to be inverted to exchange the assignment of the inputs and outputs. As shown in Fig. 3, the inverse model takes both known inputs and outputs to estimate the unknown input heat generation rate, denoted as  $\hat{\dot{Q}}$ . The estimation error  $\tilde{\dot{Q}}$  is given in the following equation:

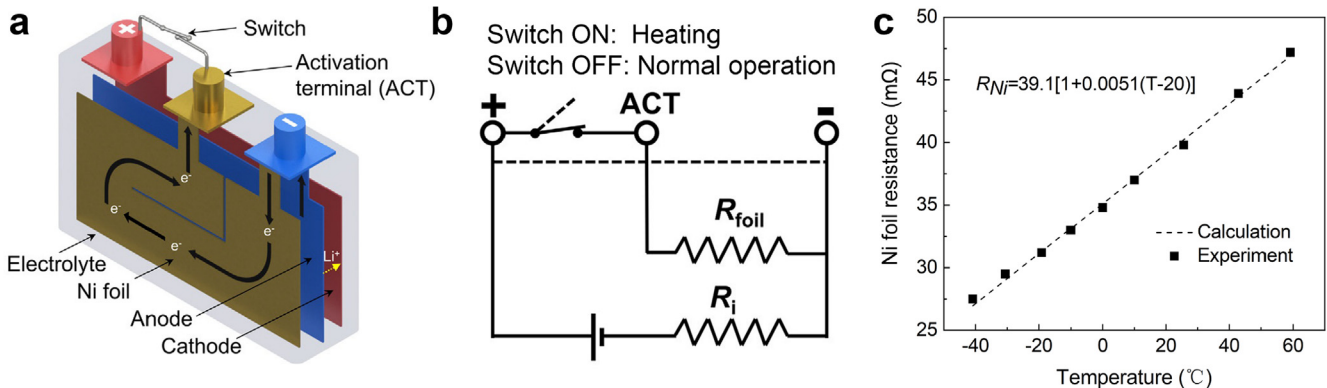


Fig. 1. [24] (a) Illustration of the SHLB structure (b) Equivalent circuit that illustrates the SHLB heating mechanism (c) Linear relationship between Ni foil resistance and temperature which enables temperature sensing of the battery core area.

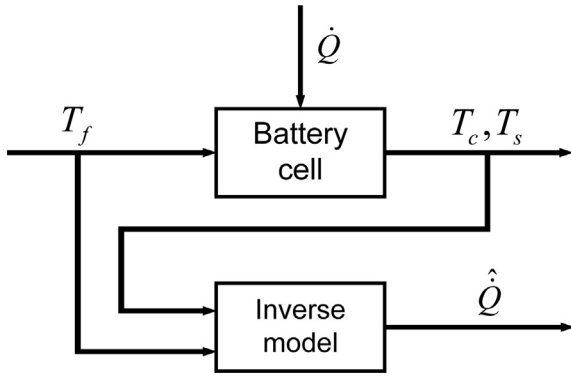


Fig. 3. Schematic of the heat generation estimation algorithm using inverse model method.

$$\tilde{Q} = \dot{Q} - \hat{Q} \quad (12)$$

An inverse heat transfer problem focuses on using measurements of the system states to determine one or several characteristics causing such states [28]. However, the inverse of a differential equation may have ill-posed solutions. Hence, to avoid this defect, the discretization technique is applied to the two-state thermal model, which transforms the ordinary differential equations into linearized algebraic equations. After the discretization with zero-order hold, the governing equations of the two-state thermal model (Eqs. (10) and (11)) turn into the following:

$$T_{c,k+1} = T_{s,k} + \dot{Q}_k R_c - \exp\left(-\frac{\Delta t}{C_c R_c}\right)(T_{s,k} - T_{c,k} + \dot{Q}_k R_c) \quad (13)$$

$$T_{s,k+1} = \frac{R_c T_{f,k} + R_u T_{c,k} - \exp\left(-\frac{\Delta t}{R_c + R_u}\right)}{(R_c + R_u)[C_s R_c R_u (R_c T_{f,k} - R_c T_{s,k} + R_u T_{c,k} - R_u T_{s,k})]} \quad (14)$$

where the subscript  $k$  stands for values from the  $k^{th}$  sampling and  $\Delta t$  is the sampling interval.

From the discretized two-state thermal model, it is noted that the heat generation rate can be deduced by only using Eq. (13) with algebraic operations. Subsequently, the estimated heat generation rate for the  $k^{th}$  step is expressed as:

$$\hat{Q}_k = \frac{T_{c,k+1} - T_{c,k} \exp\left(-\frac{\Delta t}{C_c R_c}\right) - T_{s,k} \left[1 - \exp\left(-\frac{\Delta t}{C_c R_c}\right)\right]}{R_c \left[1 - \exp\left(-\frac{\Delta t}{C_c R_c}\right)\right]} \quad (15)$$

With the presented inverse model, the heat generation estimation process is listed in Table 1.

It can also be noticed that  $T_f$  and  $R_u$  terms are absent from the heat generation estimation equation, Eq. (15). Therefore, the estimation algorithm will not be affected by thermal boundary conditions, i.e., ambient temperature and convection conditions. This feature comes from the fact that the surface temperature measurement already contains the information from the thermal boundary. This characteristic is very important for the feasibility and robustness of the heat generation estimation algorithm, because some thermal boundary conditions can change from time to time, and in most cases, are hard to be tracked, especially for onboard applications. Examples are a battery system

Table 1  
Heat generation estimation process.

Steps	Content
Step 1	At time step $k$ , measurement of $T_c$ and $T_s$ are updated and held for the $k + 1^{th}$ estimation.
Step 2	At time step $k + 1$ , measurement value of $T_c$ and $T_s$ are updated and held for the $k + 1^{th}$ and $k + 2^{th}$ estimation.
Step 3	At time step $k + 1$ , $k^{th}$ and $k + 1^{th}$ measurements of $T_c$ and $T_s$ are taken by the heat generation estimation algorithm and update the estimation of $\hat{Q}_k$ .

equipped with a fan cooling system where the fan speed is adjustable or a liquid cooling system that starts to operate from idle mode. Although empirical values of convective heat transfer coefficient are often utilized for approximate analysis, however, when it comes to quantitative estimation, such a method can cause significant errors. Therefore, the robustness against dependency on thermal boundary conditions is important for the online heat generation estimation algorithm.

Certain simplifications and assumptions made in the algorithm are worthy noting:

- (a) Measurement noises are not considered;
- (b) The temperature dependency of the two-state thermal model parameters is neglected.

It should also be noted that despite the estimation equation Eq. (15) does not rely on ambient temperatures; thermal properties of the battery can vary with temperature changes. Hence, two-state thermal model parameters can be identified for different temperature ranges if necessary.

## 4. Results & discussion

### 4.1. Two-state thermal model parameter identification

Before digging into the estimation results of heat generation, the two-state thermal model needs to be parameterized. Here, the proposed ECT model is exploited to generate the necessary data set. A stepwise heat power profile of 5 W is designed as the input to the ECT model, see Fig. 4a. The ECT model output data of core and surface temperature corresponding to this stepwise heat generation profile are recorded, as plotted in Fig. 4b. Eventually, the parametrization data set can be composed of the heat generation input and two temperature outputs. It can be noted that, during this heating period, the battery cell is neither charged nor discharged; therefore, no electrochemical heating occurs. It is also worth noting that such an approach can also be realized experimentally with SHLB. The simulation is conducted under an ambient temperature of 25°C with natural air convection, where the convective transfer coefficient is chosen as  $h = 7W/(m^2 \cdot K)$ . The initial temperature of the battery cell is also 25°C.

In order to identify the optimum parameters, the particle swarm optimization (PSO) algorithm [29,30] is adopted here, which has the advantage of good capability for global optimization and easy implementation. The algorithm works with a group of particles standing for the solution vectors, which are located in the problem space with random initial values. Along with the iteration proceeds, particles are moving towards the global minimum, driven by the cost function  $J$ . While a particle is approaching the optimum solution, the velocity  $v$  and position  $x$  are updated every iteration step using the following equations, respectively:

$$v_i^{k+1} = wv_i^k + c_1(p_i^k - x_i^k) + c_2(g_i^k - x_i^k) \quad (16)$$

$$x_i^{k+1} = x_i^k + v_i^{k+1} \quad (17)$$

where the subscription  $i$  and the  $k$  denotes the property for the  $i^{th}$  particle at  $k^{th}$  iteration,  $p$  is the particle best solution,  $g$  is the global best solution,  $w$  is the inertia constant, which is usually defined between [0.7, 0.8],  $c_1$  and  $c_2$  are acceleration constants which are set

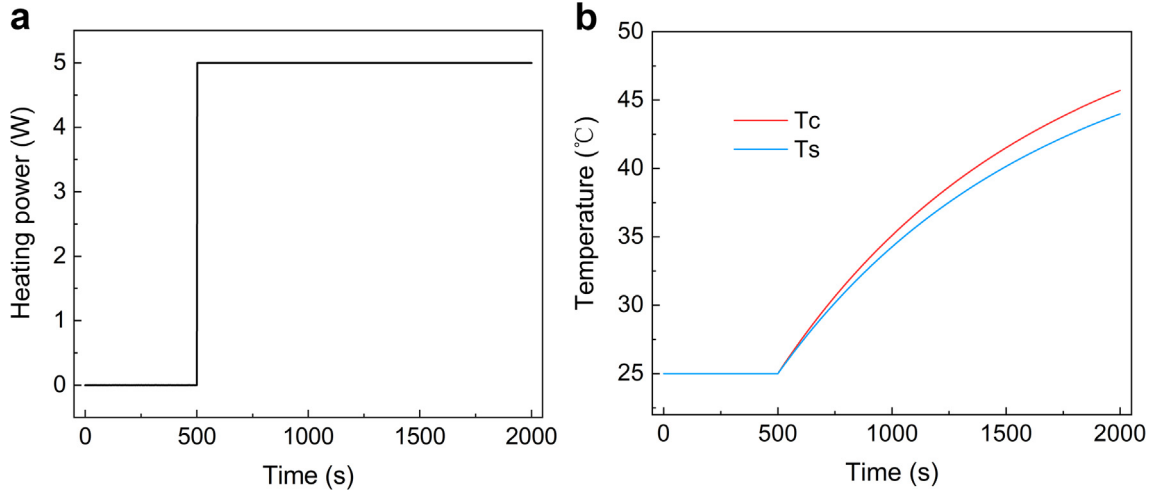


Fig. 4. Data set generated by the ECT model for two-state thermal model parameter identification (a) Input data set: heating power (b) Output data set: cell core temperature and surface temperature responses.

between[0, 2]; see Refs. [31,32].

For the two-state thermal model parameterization, the cost function  $J$  is defined in Eq. (18):

$$J = \min \left\{ \left( \frac{T_c - \hat{T}_c}{T_c} \right)^2 + \left( \frac{T_s - \hat{T}_s}{T_s} \right)^2 \right\} \quad (18)$$

where  $T_c$  and  $T_s$  are the theoretical values from the ECT model, while  $\hat{T}_c$  and  $\hat{T}_s$  are the estimation value given by the two-state thermal model. The identified parameters are listed in Table 2.

After the parameters are identified, the two-state thermal model is further applied to the Federal Urban Driving Schedule (FUDS) profile for validation, as shown in Fig. 5a. The ECT model is utilized here to simulate the electrochemical and thermal behaviors of a real battery. Under FUDS power profile, the heat generation response is recorded, and the dual-temperature responses are also stored and treated as theoretical values. The two-state thermal model takes the heat generation values to calculate the corresponding temperature responses, which are compared with theoretical values. In Fig. 5b, the theoretical value  $T$  from the ECT model and estimation value  $\hat{T}$  from the two-state thermal model of the core and surface temperatures are compared. The modeling error  $\tilde{T}$  is given as:

$$\tilde{T} = T - \hat{T} \quad (19)$$

and its results for core and surface temperatures are shown in Fig. 5c. It can be seen that the two-state thermal model matches well with the ECT model data. The maximum error is within 0.1 °C, when the battery temperature rise is around 3 °C, thus indicating a proper description of the battery thermal behavior.

#### 4.2. Algorithm evaluation

With the completely defined and parameterized two-state thermal model, it is feasible to achieve heat generation estimation with DTM inputs, using Eq. (15). In order to evaluate the performance of the presented heat generation estimation algorithm, in this subsection, two simulation cases are introduced. Case (1) is aiming to use an artificially designed heat generation profile to activate the dynamic response of the estimation algorithm. Case (2) is focusing on the simulation of battery fast charge processes, which are highly related to battery safety issues. Charging rates of 1C, 3C, and 5C are investigated.

In each case, simulations are conducted with the ECT model, through which: (1) dual-temperature measurements are acquired to be the inputs of the algorithm; (2) Heat generation rate is extracted to set a theoretical standard for algorithm evaluation. The heat generation

estimation algorithm is performed under MATLAB/Simulink™ environment.

All simulation cases are conducted under the ambient temperature of 25 °C, with the initial battery temperature of 25 °C as well. The convective heat transfer coefficient is set to  $h = 7\text{W}/(\text{m}^2\cdot\text{K})$ , mimicking a cooling condition of natural air convection.

##### 4.2.1. Designed heat generation profile case

The designed heat generation profile is composed of multiple step-wise heat generation signals with amplitudes between 1 W and 5 W, as shown detailly in Table 3. The corresponding estimation result is plotted in Fig. 6a. The black line shows the theoretical heat generation rate profile, and the red symbol describes the estimation values. It can be seen that the estimation results match well with the theoretical data, proving that the proposed algorithm can capture battery heat generation characteristics of different amplitude very well. Furthermore, during the transient process of the step change, the estimation results respond fast with unnoticeable delay.

In Fig. 6b, the estimation error and relative error are plotted. It can be noticed that, at the instant of the step change, the transient behavior can lead to spike-like estimation errors due to estimation delay. However, it can be seen that the algorithm can follow the theoretical value after seconds, which does not affect the steady-state estimation errors. Therefore, in the following text, the discussion of absolute estimation errors and relative errors excludes the initial spike effects. It can be observed from Fig. 6b that the estimation error is within  $\pm 0.06\text{W}$  range for the heat generation profile with the peak power of 5 W, or 1.2%. In addition, the relative estimation error for non-zero heat generation rates are within  $\pm 5\%$  range, and the root mean squared error (RMSE) is 0.029 W, for the entire profile duration. It can be noticed that, although the spike errors are trivial for its short period, the amplitude is high and can be harmful in digital signal processing procedures. Thus, adequate filter algorithms could be further applied to mitigate such errors.

Table 2  
Parameters of the two-state thermal model.

Parameters	Value
$C_c$	249.73 J/K
$C_s$	0.17 J/K
$R_c$	0.52 K/W
$R_u$	7.26 K/W

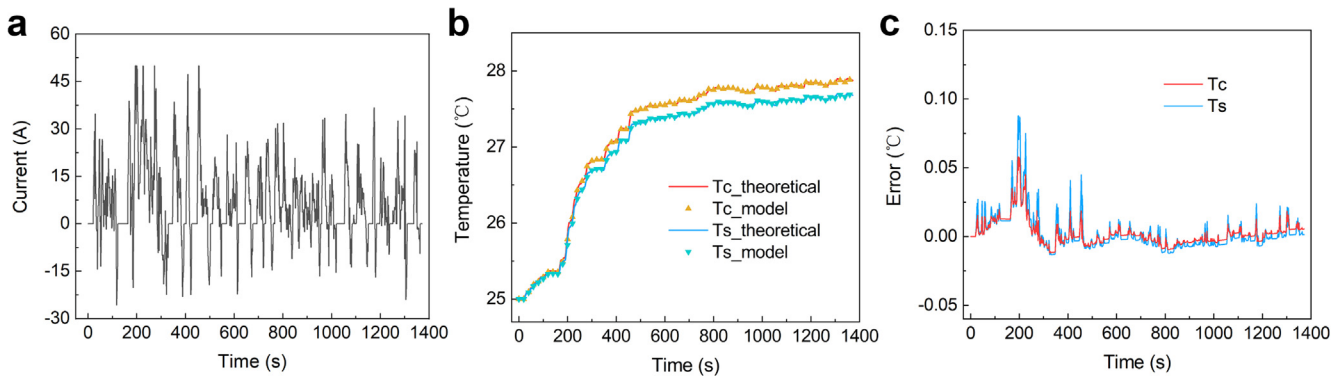


**Fig. 5.** Two-state model validation results with FUDS profile (a) FUDS current profile (b) Core temperature and surface temperature validation results (ECT model values are marked with “theoretical”, and two-state thermal model values are marked as “model”) (c) Modeling errors of the two-state thermal model.

**Table 3**

Designed heat generation rate profile.

Time (s)	Heat generation rate (W)
100	0
300	0.5
500	1
700	5
900	3
1000	0

**4.2.2. Constant current charge case**

In this subsection, cases with different C-rates of charge are examined. 1C, 3C, and 5C fast charging scenarios are selected for their considerable heat generation and greater safety concern. In these cases, the heat generation results for different C-rates are presented in Fig. 7a. The theoretical values are exported from the ECT model and shown in lines whilst the estimation values are shown in symbols. It can be found that the curves of estimation can keep good track of the theoretical ECT model in all three cases. In order to evaluate quantitatively, estimation errors and relative errors for each subcase are plotted in Fig. 7b–d and observed within  $\pm 0.05W$ ,  $\pm 0.1W$  and  $\pm 0.2W$  range for 1C, 3C, and 5C charge rate cases, respectively. Moreover, the relative estimation errors for 1C, 3C, and 5C cases are within  $\pm 10\%$ ,  $\pm 2.5\%$  and  $\pm 2\%$  range after a short initial fluctuation. In addition, the RMSE are 0.010 W, 0.029 W and 0.029 W each. It can be seen that, with a larger current, which also means a larger heat generation rate, the absolute error increases, but the relative error further decreases. This indicates the absolute error grows with the signal amplitude, but the degree of growth

of absolute error is smaller than that of the signal amplitude. Therefore, the estimation method could be more accurate for large heat generation cases.

It can be concluded that the case study shows a precise estimation performance of the algorithm under fast charging circumstances. By doing so, battery charging safety can be further monitored, and thermal runaway accidents may be prevented by further taking advantage of such a fault detection technique.

**4.3. Effects of different convection conditions**

From the expression presented in Eq. (15), one can see that the heat generation estimation algorithm works regardless of the thermal boundary conditions. In this subsection, the effects of different convection conditions are simulated and discussed; the robustness of the algorithm is verified.

In order to evaluate the estimation performance against changes in convection conditions, three cases are employed with different convective heat transfer coefficients,  $h$ . The base case that simulates the natural air convection case with  $h = 7W/(m^2 \cdot K)$  has already been shown in the previous Section 4.2.1. After that, case (1) uses  $h = 20W/(m^2 \cdot K)$  to realize an air turbulent flow situation and case (2) utilizes  $h = 57W/(m^2 \cdot K)$  to study the case of liquid cooling condition [33]. All three cases use the same set of two-state model parameters, as displayed in Table 2, which are identified under the base case condition.

In this case study, the designed multi-stepwise heat generation profile is adopted for the ECT simulation rather than a current input profile. The reason is that battery heat generation caused by its

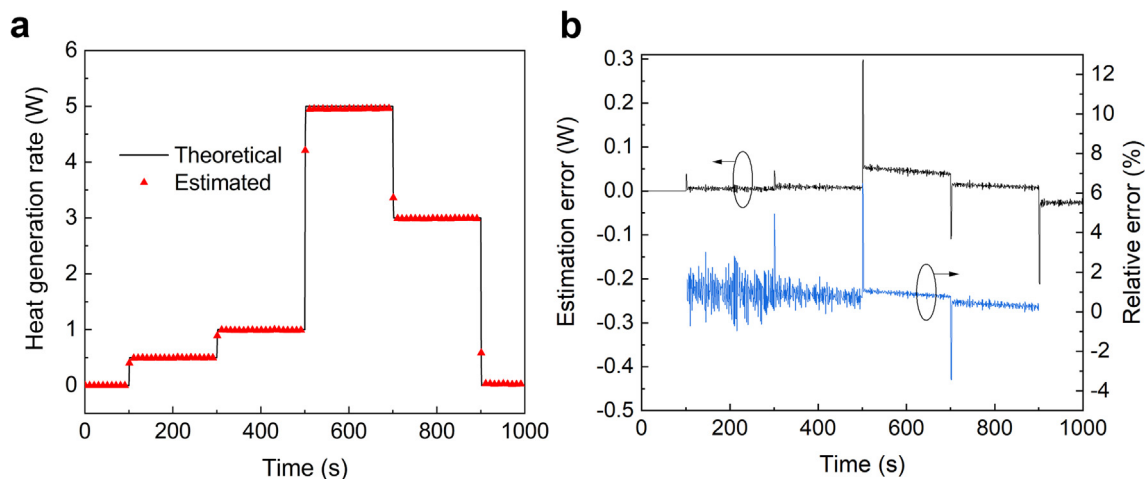


**Fig. 6.** (a) Estimation result for the designed heat generation profile (b) Estimation error and relative error.

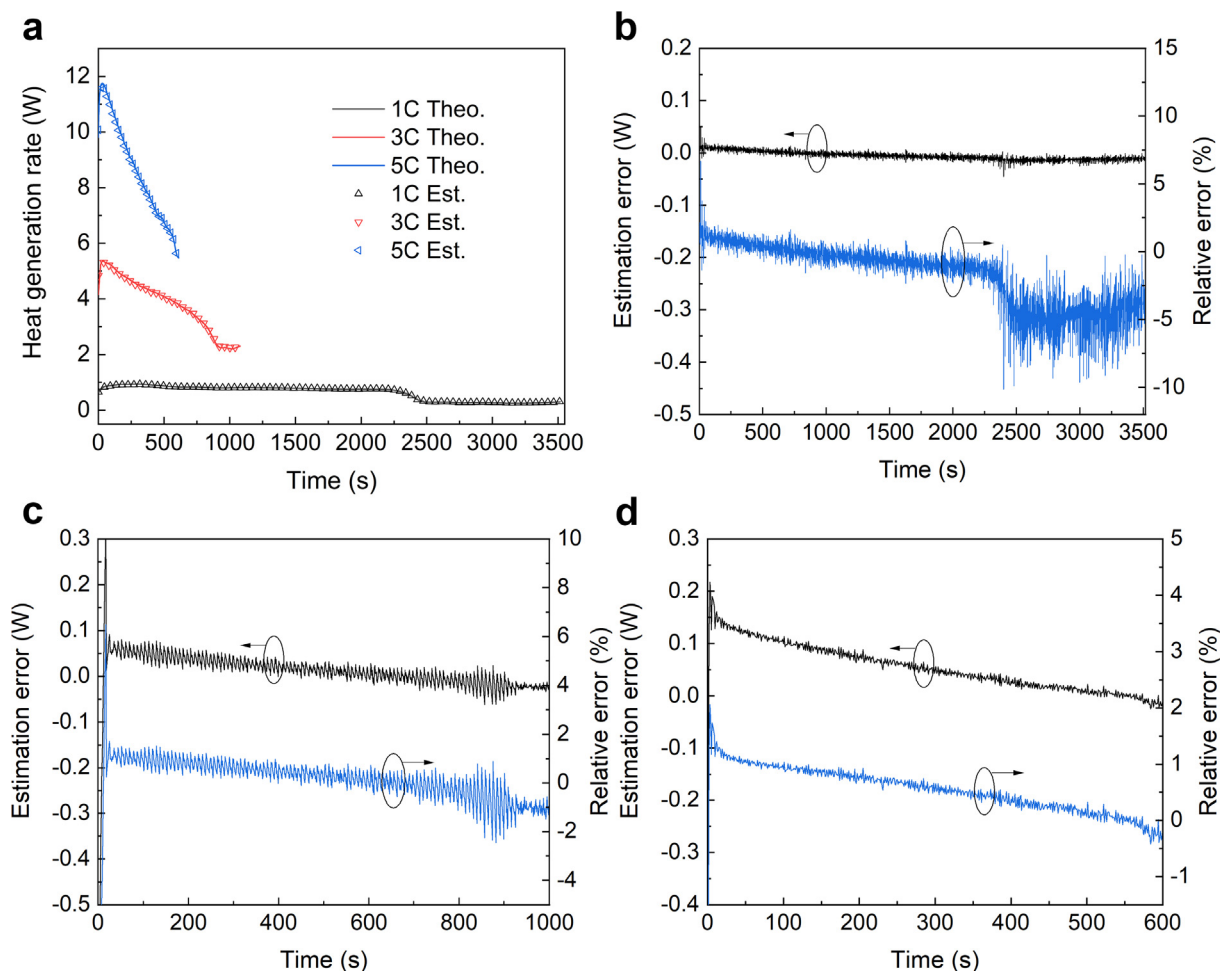


Fig. 7. (a) Estimation results for constant current charge with 1C, 3C and 5C rates (b) Estimation error and relative error for 1C charge (c) Estimation error and relative error for 3C charge (d) Estimation error and relative error for 5C charge.

electrochemical reaction is highly coupled with temperature, which can be further influenced by different thermal boundary conditions. Therefore, such an effect can lead to incomparability between cases. Using a defined heat generation profile could eliminate this problem and decouple the heat generation rate from cell temperature, thus achieving valid comparisons.

As can be seen from Fig. 8a and c, with a wide range of convection conditions, the estimation results for case (1) and (2) still show excellent match of the given heat generation rate profile and perform uniformly with the base case, which proves the independency on heat convection condition of the algorithm. In addition, as shown in Fig. 8b and d, estimation errors are within  $\pm 0.1$ W range, while the amplitude range of the theoretical value is from 0 W to 5 W, except for the spike-like errors. The relative estimation error for non-zero heat generation rate values in case (1) and (2) are both within  $\pm 3\%$ , and the RMSEs are 0.017 W and 0.022 W each. The error ranges are quite small and also at the same level as the base case, where the absolute error, relative error, and RMSE are within  $\pm 0.06$ W,  $\pm 5\%$  range, and 0.027 W, respectively.

#### 4.4. Effects of cell thickness

To date, EV type batteries are characterized by high energy density and high capacity. High-capacity active materials meet such needs on one hand. On the other hand, thick electrodes are used and cell thickness and volume increase. For large scale batteries, the internal temperature distribution can be non-uniform, hence whether the two-state model is applicable to those EV batteries of different thickness is an

open question.

As introduced earlier in Section 3.2, the two-state thermal model is an improved lumped model. Therefore, in this subsection, simulation evaluation is conducted to perceive if cells with different thicknesses can be well modeled. Other than the base case cell thickness of 10 mm, the study is extended to cover cell thicknesses of 30 mm and 50 mm. It is worth noting that, with the increase of cell thickness, a cell also gains more thermal mass. Therefore, parameters for each cell thickness are re-identified using the same method introduced in Section 4.1. The identified parameters are presented in Table 4. The validation method is identical to that used in Section 4.3. Fig. 9a and c show the estimation results for both 30 mm- and 50 mm-thick cells by using respective models. It can be seen that, although subject to the assumption of only two thermal states, the model still shows excellent estimation performance for the above-studied cell thicknesses, which can cover a large portion of EV type battery cells. The estimation errors for both cases, as shown in Fig. 9b and d, are within  $\pm 0.05$ W and the relative estimation errors for non-zero heat generation rate are within  $\pm 6\%$  and  $\pm 8\%$  for 30 mm- and 50 mm-thickness case, respectively, and the RMSEs are 0.012 W and 0.014 W each. Although it can be noticed that the estimation fluctuations for thicker cells become more apparent, probably due to larger heat capacity. The algorithm can still follow with reasonable precision, with low overall RMSE. Under this circumstance, measurement noise could become more significant in practice and therefore need to be controlled by filtering techniques.

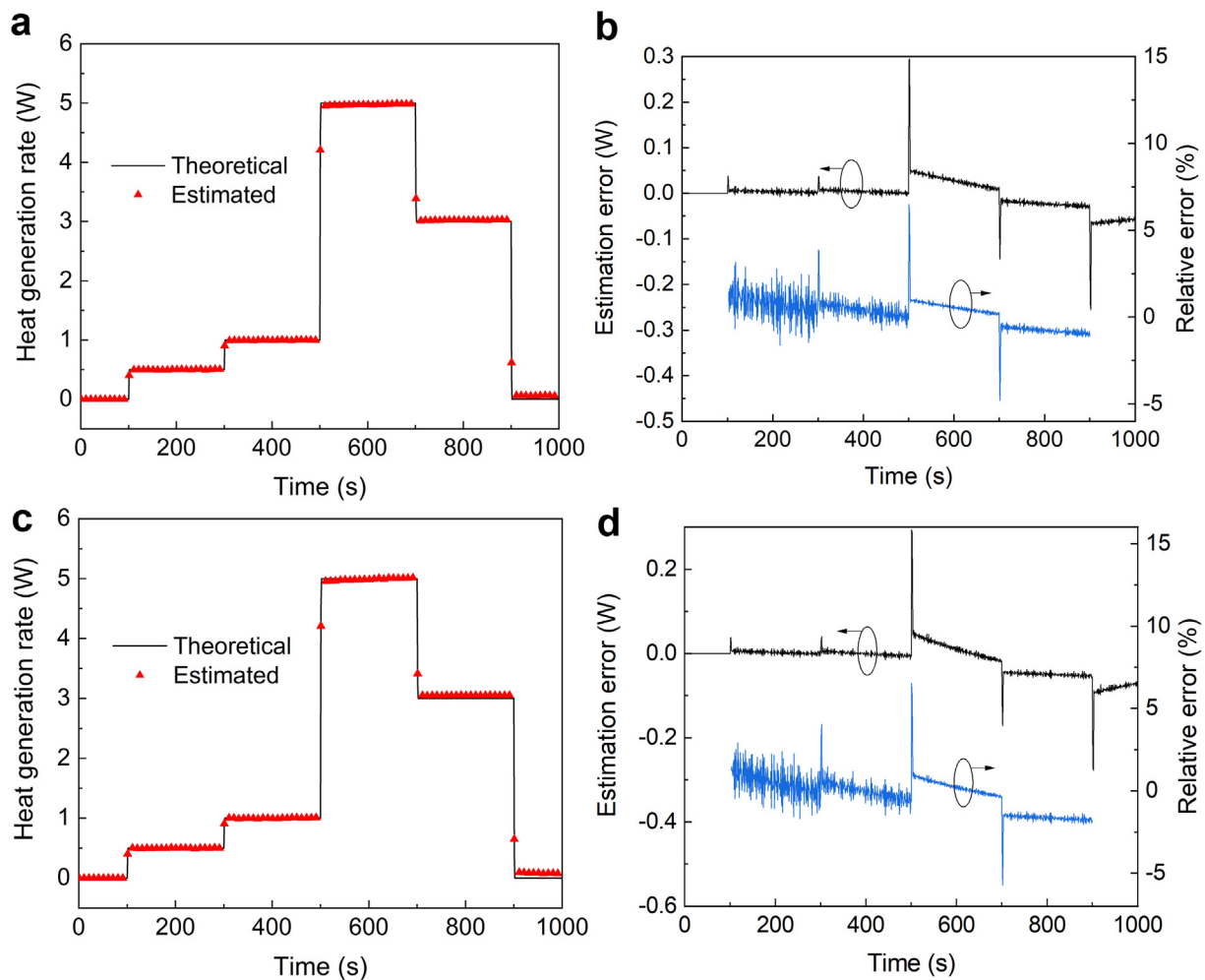


**Fig. 8.** Estimation results under different cooling conditions **Case (1):** convective heat transfer coefficient of 25 W/(m<sup>2</sup>K) for turbulent air cooling (a) Heat generation estimation result (b) Estimation error and relative error **Case (2):** convective heat transfer coefficient of 57 W/(m<sup>2</sup>K) for liquid cooling (c) Heat generation estimation result (d) Estimation error and relative error.

**Table 4**  
Two-state thermal model parameters identified for different cell thicknesses.

Parameters	30 mm	50 mm
$C_c$	756.53 J/K	1275.6 J/K
$C_s$	0.15 J/K	0.14 J/K
$R_c$	1.54 K/W	3.13 K/W
$R_u$	7.09 K/W	8.64 K/W

**5. Conclusions**

We have presented an online heat generation estimation method for lithium-ion battery cells, based on dual-temperature measurement and a two-state thermal model with high accuracy, robustness, and generalizability. The DTM method is proposed to: (1) turn the internal temperature into an accessible measurement for online applications; and (2) deal with the temperature gradient inside a battery. Subsequently, the two-state thermal model has been adopted to derive the heat generation estimation equation with discretization and inverse model techniques.

Through computational studies using the experimentally calibrated ECT model, the effectiveness of the proposed heat generation estimation algorithm has been validated with both designed heat generation rate profile case and fast charging cases. In the designed heat generation rate profile case, the proposed algorithm could keep good track of

multiple step-wise signals with different amplitudes, where the relative estimation error was  $\pm 5\%$ , and RMSE was 0.027 W. Due to the highly focused safety issue during fast charging, cases of 1C, 3C, and 5C charging rates are investigated, where the presented algorithm can keep the relative estimation error within  $\pm 10\%$ ,  $\pm 2.5\%$  and  $\pm 2\%$  range and RMSE of 0.010 W, 0.029 W and 0.029 W for each case. It is found that the algorithm could attain better accuracy for higher C-rates, which are riskier occasions demanding thermal fault detection.

Robustness of the algorithm is also verified under different convection conditions. Good prediction of the given heat generation rate is demonstrated for the natural air convection, turbulent air cooling, and liquid cooling scenarios. Except for the base case of natural convection, the relative estimation errors are all within  $\pm 3\%$  range, and the RMSEs are 0.017 W and 0.022 W for turbulent air cooling and liquid cooling conditions, respectively, showing adequate robustness against changes in convection conditions. Moreover, the generalizability to thick battery cells has also been evaluated. With individually identified parameters, 30 mm- and 50 mm-thick battery cells are simulated. Supported by the relative estimation errors within  $\pm 8\%$  and the RMSEs of 0.012 W and 0.014 W for 30 mm and 50 mm case, the algorithm can be generalized to a wide range of battery thickness designs.

There are three advantages arising from the present method: (1) Heat generation can be estimated regardless of its source; thus, the abnormal heat generation can be included, which is valuable for improving battery safety. (2) No knowledge of thermal conditions is required, further achieving the robustness against thermal boundary

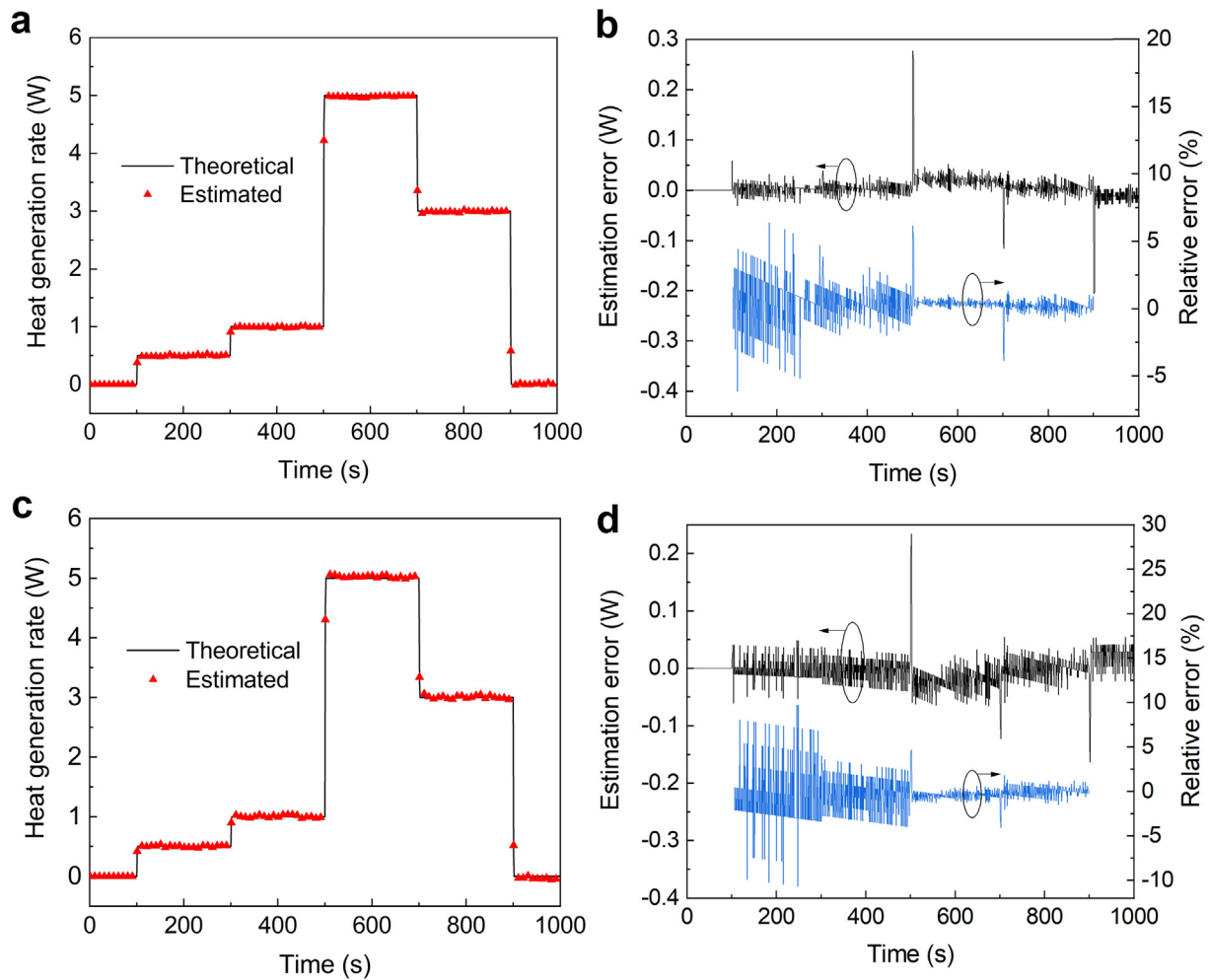


Fig. 9. Estimation results with different cell thicknesses using two-state thermal model parameters shown in Table 4 for each case. Case (1): 30 mm cell thickness (a) Heat generation estimation result (b) Estimation error and relative error Case (2): 50 mm cell thickness (c) Heat generation estimation result (d) Estimation error and relative error.

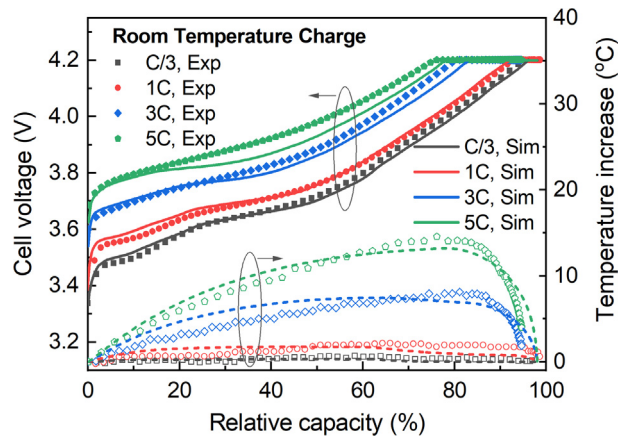


Fig. A1. Room temperature charge validation.

condition variations. (3) The algorithm can be generalized to different battery cell designs. Also, while the present work is focused solely on single cells, the present heat generation estimation method is expected to be applicable to battery modules and packs. This is because the DTM method is rooted in the SHLB structure, which has already been used in modules and packs deployed in real-world vehicles [34].

Nevertheless, there are still deficiencies in the present method

which need to be addressed in future work. The method requires further experimental evaluation in a physical build. Also, measurement noises are not considered in this study but can become challenging in practice. Therefore, online noise reduction and filtering methods need to be exploited in future research.

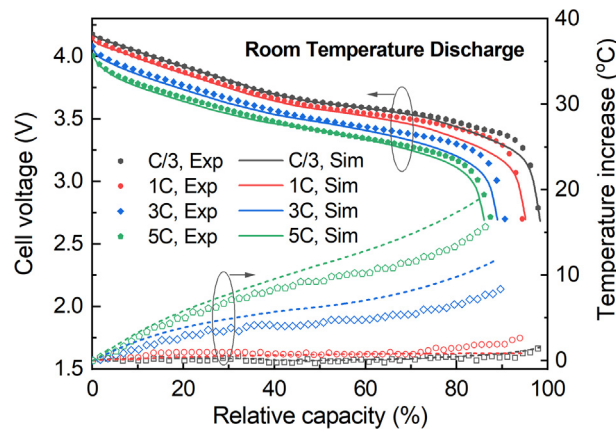


Fig. A2. Room temperature discharge validation.

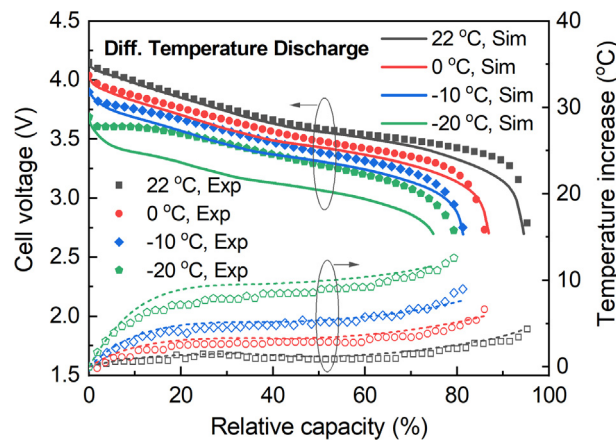


Fig. A3. 1C discharge validation under different temperatures.

**CRedit authorship contribution statement**

**Jianan Zhang:** Conceptualization, Methodology, Software, Visualization, Investigation, Writing - original draft, Writing - review & editing. **Xiao-Guang Yang:** Validation, Writing - review & editing. **Fengchun Sun:** Supervision. **Zhenpo Wang:** Supervision. **Chao-Yang Wang:** Supervision, Writing - review & editing.

**Declaration of Competing Interest**

The authors declare that they have no known competing financial

interests or personal relationships that could have appeared to influence the work reported in this paper.

**Acknowledgment**

JZ, FS, and ZW acknowledge partial support of this work by the State Key Program of the National Natural Science Foundation of China under Grant U1564206, and JZ is further supported in part by the China Scholarship Council under Grant 201706030101. We are also grateful to Gamma Technologies for offering GT-AutoLion™ software.

**Appendix A. Electrochemical-thermal model validation against experimental results**

See Figs. A1–A3.

**References**

- [1] Zhang J, Zhang L, Sun F, Wang Z. An overview on thermal safety issues of lithium-ion batteries for electric vehicle application. *IEEE Access* 2018;6:23848–63.
- [2] Zhang J, Huang J, Li Z, Wu B, Nie Z, Sun Y, et al. Comparison and validation of methods for estimating heat generation rate of large-format lithium-ion batteries. *J Therm Anal Calorim* 2014;117:447–61.
- [3] Manikandan B, Yap C, Balaya P. Towards understanding heat generation characteristics of Li-ion batteries by calorimetry, impedance, and potentiometry studies. *J Electrochem Soc* 2017;164:A2794–800.
- [4] Farag M, Sweity H, Fleckenstein M, Habibi S. Combined electrochemical, heat generation, and thermal model for large prismatic lithium-ion batteries in real-time applications. *J Power Sources* 2017;360:618–33.
- [5] Chen K, Unsworth G, Li X. Measurements of heat generation in prismatic Li-ion batteries. *J Power Sources* 2014;261:28–37.
- [6] Drake SJ, Martin M, Wetz DA, Ostanek JK, Miller SP, Heinzel JM, et al. Heat generation rate measurement in a Li-ion cell at large C-rates through temperature and heat flux measurements. *J Power Sources* 2015;285:266–73.
- [7] Bernardi D, Pawlikowski E, Newman J. A general energy balance for battery systems. *J Electrochem Soc* 1985;132:5–12.
- [8] Rao L, Newman J. Heat-generation rate and general energy balance for insertion battery systems. *J Electrochem Soc* 1997;144:2697–704.
- [9] Greco A, Cao D, Jiang X, Yang H. A theoretical and computational study of lithium-ion battery thermal management for electric vehicles using heat pipes. *J Power Sources* 2014;257:344–55.
- [10] Rao Z, Wang S, Zhang G. Simulation and experiment of thermal energy management with phase change material for ageing LiFePO4 power battery. *Energy Convers Manage* 2011;52:3408–14.
- [11] Xie Y, Shi S, Tang J, Wu H, Yu J. Experimental and analytical study on heat generation characteristics of a lithium-ion power battery. *Int J Heat Mass Transf* 2018;122:884–94.

- [12] Zhang G, Cao L, Ge S, Wang C-Y, Shaffer CE, Rahn CD. Reaction temperature sensing (RTS)-based control for Li-ion battery safety. *Sci Rep* 2015;5:18237.
- [13] Srinivasan R, Carkhuff BG, Butler MH, Baisden AC. Instantaneous measurement of the internal temperature in lithium-ion rechargeable cells. *Electrochim Acta* 2011;56:6198–204.
- [14] Kim Y, Mohan S, Siegel JB, Stefanopoulou AG, Ding Y. The estimation of temperature distribution in cylindrical battery cells under unknown cooling conditions. *IEEE Trans Control Syst Technol* 2014;22:2277–86.
- [15] Li Z, Zhang J, Wu B, Huang J, Nie Z, Sun Y, et al. Examining temporal and spatial variations of internal temperature in large-format laminated battery with embedded thermocouples. *J Power Sources* 2013;241:536–53.
- [16] Wang C-Y, Zhang G, Ge S, Xu T, Ji Y, Yang X-G, et al. Lithium-ion battery structure that self-heats at low temperatures. *Nature* 2016;529:515.
- [17] Gamma Technologies. GT-AutoLion; 2019. Available from: <https://www.gtisoft.com/gt-autolion/>.
- [18] Gu WB, Wang CY. Thermal-electrochemical modeling of battery systems. *J Electrochem Soc* 2000;147:2910–22.
- [19] Ji Y, Zhang Y, Wang C-Y. Li-ion cell operation at low temperatures. *J Electrochem Soc* 2013;160:A636–49.
- [20] Yang X-G, Zhang G, Wang C-Y. Computational design and refinement of self-heating lithium ion batteries. *J Power Sources* 2016;328:203–11.
- [21] Al Hallaj S, Maleki H, Hong JS, Selman JR. Thermal modeling and design considerations of lithium-ion batteries. *J Power Sources* 1999;83:1–8.
- [22] Zhang J, Wu B, Li Z, Huang J. Simultaneous estimation of thermal parameters for large-format laminated lithium-ion batteries. *J Power Sources* 2014;259:106–16.
- [23] Yang X-G, Zhang G, Ge S, Wang C-Y. Fast charging of lithium-ion batteries at all temperatures. *Proc Natl Acad Sci* 2018;115:7266–71.
- [24] Zhang G, Ge S, Xu T, Yang X-G, Tian H, Wang C-Y. Rapid self-heating and internal temperature sensing of lithium-ion batteries at low temperatures. *Electrochim Acta* 2016;218:149–55.
- [25] Lin X, Perez HE, Siegel JB, Stefanopoulou AG, Li Y, Anderson RD, et al. Online parameterization of lumped thermal dynamics in cylindrical lithium ion batteries for core temperature estimation and health monitoring. *IEEE Trans Control Syst Technol* 2013;21:1745–55.
- [26] Dey S, Biron ZA, Tatipamula S, Das N, Mohon S, Ayalew B, et al. Model-based real-time thermal fault diagnosis of Lithium-ion batteries. *Control Eng Pract* 2016;56:37–48.
- [27] Zhang D, Dey S, Perez HE, Moura SJ. Real-time capacity estimation of lithium-ion batteries utilizing thermal dynamics. *IEEE Trans Control Syst Technol* 2020;28:992–1000.
- [28] Alifanov OM. Inverse heat transfer problems. Springer Science & Business Media; 2012.
- [29] Eberhart, Yuhui S. Particle swarm optimization: developments, applications and resources. In: *Proceedings of the 2001 Congress on Evolutionary Computation (IEEE Cat No01TH8546)2001*, vol. 1. p. 81–6.
- [30] Venter G, Sobieszcanski-Sobieski J. Particle swarm optimization. *AIAA J* 2003;41:1583–9.
- [31] Rahman MA, Anwar S, Izadian A. Electrochemical model parameter identification of a lithium-ion battery using particle swarm optimization method. *J Power Sources* 2016;307:86–97.
- [32] Long B, Xian W, Jiang L, Liu Z. An improved autoregressive model by particle swarm optimization for prognostics of lithium-ion batteries. *Microelectron Reliab* 2013;53:821–31.
- [33] Pesaran AA. Battery thermal management in EV and HEVs: issues and solutions. *Battery Manage* 2001;43:34–49.
- [34] Yang X, Ge S, Wu N, Mao Y, Sun F, Wang C. All-climate battery technology for electric vehicles: inching closer to the mainstream adoption of automated driving. *IEEE Electr Mag* 2019;7:12–21.